AGU PUBLICATIONS

Geophysical Research Letters

RESEARCH LETTER
10.1002/2017GL073406

Key Points:
- Isotope-enabled CESM simulations suggest that ENSO variability at the LGM is most likely weaker than that of the preindustrial
- Total variance from some IFA reconstructions may only reflect changes in the annual cycle instead of ENSO variability
- Habitat depth of subsurface foraminifera and their vertical migration can complicate interpretations of subsurface IFA reconstructions

Supporting Information:
- Supporting Information S1

Correspondence to:
J. Zhu,
jzhu47@wisc.edu

Citation:
Zhu, J., et al. (2017), Reduced ENSO variability at the LGM revealed by an isotope-enabled Earth system model, *Geophys. Res. Lett.*, *44*, 6984–6992, doi:10.1002/2017GL073406.

Received 10 MAR 2017
Accepted 19 JUN 2017
Accepted article online 20 JUN 2017
Published online 12 JUL 2017

©2017. American Geophysical Union. All Rights Reserved.

Reduced ENSO variability at the LGM revealed by an isotope-enabled Earth system model

Jiang Zhu[1], Zhengyu Liu[1], Esther Brady[2], Bette Otto-Bliesner[2], Jiaxu Zhang[1,3], David Noone[4], Robert Tomas[2], Jesse Nusbaumer[5], Tony Wong[6], Alexandra Jahn[7], and Clay Tabor[2]

[1]Department of Atmospheric and Oceanic Sciences and Center for Climatic Research, University of Wisconsin-Madison, Madison, Wisconsin, USA, [2]Climate and Global Dynamics Division, National Center for Atmospheric Research, Boulder, Colorado, USA, [3]Now at Los Alamos National Laboratory, Los Alamos, New Mexico, USA, [4]College of Earth, Ocean, and Atmospheric Sciences, Oregon State University, Corvallis, Oregon, USA, [5]NASA Goddard Institute for Space Studies, New York, New York, USA, [6]Earth and Environmental Systems Institute, Pennsylvania State University, University Park, Pennsylvania, USA, [7]Department of Atmospheric and Oceanic Sciences and Institute of Arctic and Alpine Research, University of Colorado Boulder, Boulder, Colorado, USA

Abstract Studying the El Niño–Southern Oscillation (ENSO) in the past can help us better understand its dynamics and improve its future projections. However, both paleoclimate reconstructions and model simulations of ENSO strength at the Last Glacial Maximum (LGM; 21 ka B.P.) have led to contradicting results. Here we perform model simulations using the recently developed water isotope-enabled Community Earth System Model (iCESM). For the first time, model-simulated oxygen isotopes are directly compared with those from ENSO reconstructions using the individual foraminifera analysis (IFA). We find that the LGM ENSO is most likely weaker comparing with the preindustrial. The iCESM suggests that total variance of the IFA records may only reflect changes in the annual cycle instead of ENSO variability as previously assumed. Furthermore, the interpretation of subsurface IFA records can be substantially complicated by the habitat depth of thermocline-dwelling foraminifera and their vertical migration with a temporally varying thermocline.

1. Introduction

El Niño–Southern Oscillation (ENSO), the oscillating warm and cold events at interannual time scale in the eastern equatorial Pacific Ocean (EEP), has widespread impacts on the global climate, ecological, and socioeconomic systems [*Philander*, 1990; *Liu and Alexander*, 2007]. Despite its paramount importance in the climate system, the projected response of the ENSO variability to the anthropogenic global warming in current climate models is still highly inconclusive and model-dependent [*Intergovernmental Panel on Climate Change* (*IPCC*) *et al*., 2013]. Reconstructions of past climate can serve as a test bed for these climate models and provide us the opportunity to study the relationship between ENSO variability and the background climate states [*Tudhope*, 2001; *Cobb et al*., 2003, 2013; *Carre et al*., 2014]. However, there is still substantial discrepancy in paleoclimate records [*Leduc et al*., 2009; *Wolff et al*., 2011; *Koutavas and Joanides*, 2012; *Sadekov et al*., 2013; *Ford et al*., 2015] regarding the ENSO variability at the Last Glacial Maximum (LGM; 21,000 years ago), a cold period during the last ice age when ice sheets were at their greatest extent and the CO_2 concentration was ~100 parts per million lower [*Clark et al*., 2009]. For instance, using the individual foraminifera analysis (IFA) approach, some oxygen isotope reconstructions from the EEP suggest a stronger ENSO than that of the preindustrial [*Koutavas and Joanides*, 2012; *Sadekov et al*., 2013], while others indicate a weaker ENSO [*Leduc et al*., 2009].

The problem is further complicated by the fact that coupled climate models also do not agree on the ENSO strength at the LGM [*Otto-Bliesner*, 2003; *Otto-Bliesner et al*., 2006; *Zheng et al*., 2008; *Brady et al*., 2013], although the multimodel median shows a slightly weaker ENSO [*IPCC et al*., 2013]. Furthermore, conventional climate models can only simulate climate state variables (e.g., ocean temperature) instead of the proxy variables (e.g., oxygen isotopes), making the traditional approach of model-data comparison an indirect one. Additionally, both the models and reconstructions are subject to substantial biases and uncertainties [*Ravelo and Hillaire-Marcel*, 2007; *Bellenger et al*., 2014], leading to contradictions in models and reconstructions that are difficult to address.

In this study, we make the first direct comparison between modeling results and available oxygen isotope ($\delta^{18}O$) records with a focus on the ENSO variability at the LGM, using the recently developed water isotope-enabled Community Earth System Model (iCESM). By assessing uncertainties in oxygen isotope proxies and combining evidence from both reconstructions and models, we find that the ENSO strength is most likely weaker at the LGM comparing with the preindustrial. Regarding $\delta^{18}O$-IFA records in the EEP, the iCESM simulations indicate that the total variance from these records may only reflect changes in the annual cycle instead of the ENSO variability. It is further pointed out that interpretations of subsurface IFA records could be substantially complicated by the uncertainties in the habitat depth of the thermocline-dwelling foraminifera and their tendency to migrate vertically with a temporally varying thermocline.

2. Model and Experiments

The model employed in this study is the recently developed isotope-enabled Community Earth System Model (CESM) version 1.3. Although being an experimental release, it has a similar physical climate as the CESM1 [*Hurrell et al*., 2013]. In addition to the regular hydrologic cycle, iCESM can explicitly simulate the transport and transformation of water isotopes (e.g., $H_2{}^{18}O$) in its components—the atmosphere, land, ocean, sea ice, and river runoff. The description of the individual components including the isotope-enabled atmosphere, land, and ocean models are documented elsewhere [*Nusbaumer et al*., 2017; *Wong et al*., 2017; *Zhang*, 2016]. Note that similar experiments were also carried out using the isotope-enabled CESM version 1.2 (an official public release version), and major conclusions are qualitatively unchanged (Table S1 and Text S1 in the supporting information).

Two simulations were carried out for the preindustrial and the LGM, respectively. In the preindustrial control run, all the climatic forcings were fixed at the values from A.D. 1850. The LGM simulation was conducted following the Paleoclimate Modelling Intercomparison Project version 4 (PMIP4) protocol [*Kageyama et al*., 2016], with the climatic forcings at 21 ka B.P. including the orbital parameters, lowered greenhouse gas (GHG) concentrations, increased ice sheets from the ICE-6G [*Peltier et al*., 2015], and altered land/ocean distribution to represent the effect of lowered sea level. The climate state of the LGM simulation was initialized from previous LGM simulations without water isotopes [*Brady et al*., 2013; *DiNezio et al*., 2016], which have been integrated for more than 1000 years for the climate to reach quasi-equilibrium. Ocean water isotopes in both the preindustrial and LGM simulations were initialized from the Goddard Institute for Space Studies observations [*LeGrande and Schmidt*, 2006], but a constant value of 1.05‰ was added in the LGM simulation to account for the isotopically enriched seawater caused by the increased ice sheets [*Duplessy et al*., 2002]. We ran all of the simulations with a horizontal resolution of 1.9 × 2.5° (latitude × longitude) for the atmosphere and land, and used the nominal 1° displaced pole Greenland grid for the ocean and sea ice. Both the preindustrial and LGM simulations were integrated for 500 years and the last 200 years were analyzed. A linear paleotemperature equation [*Bemis et al*., 1998] is used to calculate the modeled $\delta^{18}O$ of foraminifera shells ($\delta^{18}O_c$) from the model-simulated ocean temperature and $\delta^{18}O$ of seawater (a different paleotemperature equation [*Shackleton*, 1974] changes the results by no more than 5%).

In the present study, the total standard deviation (SD) (or variance) of sea surface temperature (SST) or oxygen isotopes is calculated from the monthly model output. The interannual SD (or variance) is calculated by the following steps. First, monthly anomalies are computed by subtracting the mean monthly climatology from the original data. Next, the linear trend is removed and a 1–2–1 filter is used to smooth the monthly anomalies. Then, SD of the monthly anomalies is calculated to represent the interannual SD. The qualitative results are not dependent on details of the calculation. The variances of the preindustrial and LGM simulations are tested using the *F* test. Thermocline depth is defined as the depth of the maximum vertical temperature gradient [*Yang and Wang*, 2009].

3. Weakened ENSO in the Simulations

The SD of tropical SST and the climatological mean SST, surface wind stress, and thermocline depth in the preindustrial simulation are compared with observations in Figures 1a–1d. The iCESM reproduces the observed mean thermal structure and wind pattern in the tropical Pacific reasonably well (Figure 1b). iCESM exhibits several issues that are common in the current generation of coupled general circulation models, including the "double Intertropical Convergence Zone" and a reduced thermocline tilt [*IPCC et al*., 2013].

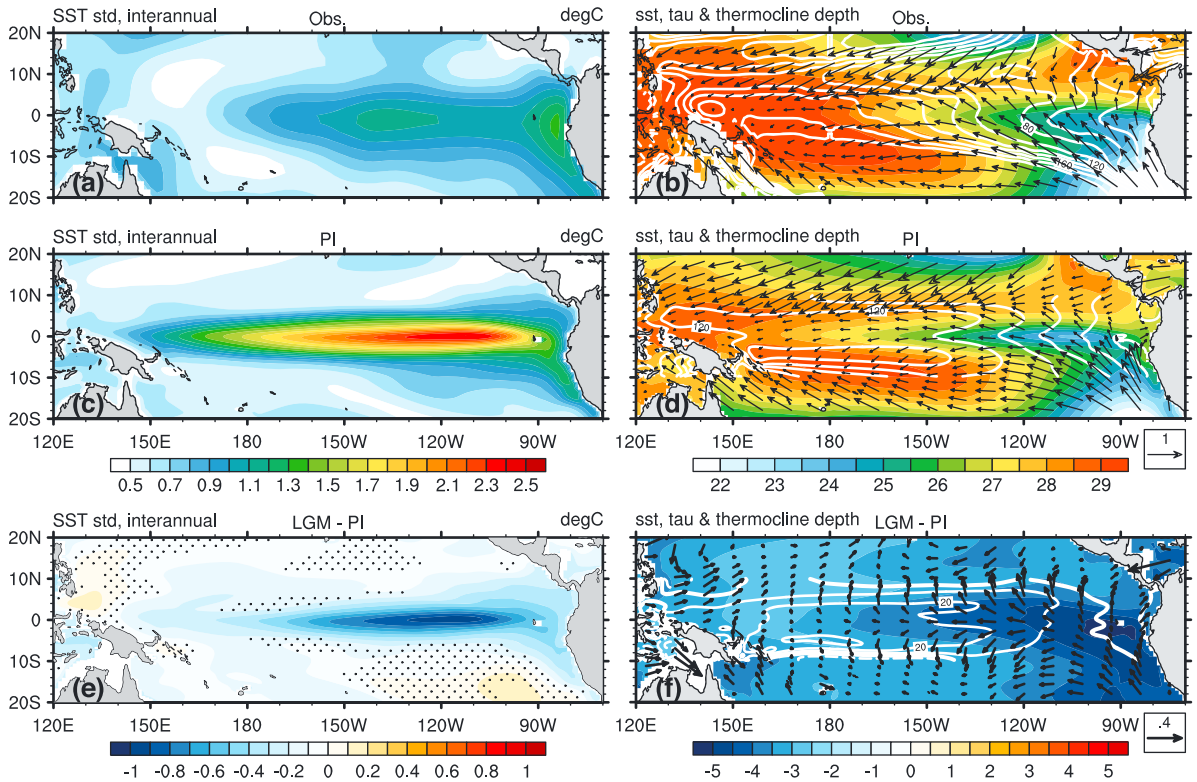

Figure 1. (a) Interannual standard deviation of sea surface temperature (SST; units: °C) in the observation from the ERSST v4 [*Huang et al.*, 2014; *W. Liu et al.*, 2014]. (b) Climatological mean SST (shading, units: °C), surface wind stress (vectors, units: N m^{-2}) from the Scatterometer Climatology of Ocean Winds [*Risien and Chelton*, 2008], and thermocline depth (white contour, units: m) calculated from the ICOADS release 3.0 [*Freeman et al.*, 2017]. (c and d) Same as in Figures 1a and 1b but for variables in the preindustrial control simulation. (e and f) Same as in Figures 1c and 1d but for changes in the LGM simulation. Differences insignificant at the 95% confidence level are dotted in Figure 1e.

The interannual SD along the equator in the iCESM is too strong when compared with observations. For example, the interannual SD in the Niño3.4 region (5°S–5°N, 170–120°W) is 1.55°C, 90% larger than observations. The bias in ENSO variability could be related to the relative coarse resolution (~2°) of the atmospheric component. It has been shown that the amplitude of interannual variability is significantly improved in simulations with higher-resolution versions of the CESM [*Deser et al.*, 2012; *Brady et al.*, 2013; *Small et al.*, 2014] (Table S1 and Text S1).

In this context, our iCESM simulations show a weakened ENSO variability at the LGM compared with the preindustrial (Figures 1c and 1e). Relative to preindustrial, the SD of SST at the interannual and longer time scale along the entire equatorial Pacific is substantially smaller at the LGM, with an average value in the Niño3.4 region decreased by 30% (from 1.55 to 1.08°C). The simulated weakened ENSO at the LGM is in qualitative agreement with previous versions of the Community Earth System Models [*Zheng et al.*, 2008; *Brady et al.*, 2013] and the median of the PMIP2 and PMIP3 models (which show a weakening around 10%) [*IPCC et al.*, 2013] (Table S1 and Text S1).

The reduced glacial ENSO variability in the model is associated with a La Niña-like cooling, intensified easterly trade winds, and a deeper thermocline in the equatorial Pacific (Figures 1d and 1f), which generally agree with relationships discovered in previous studies [*Clement et al.*, 1999; *Fedorov and Philander*, 2001; *Wang and An*, 2002; *Karnauskas et al.*, 2012; *Koutavas and Joanides*, 2012; *Sadekov et al.*, 2013; *Ford et al.*, 2015]. There is an enhanced equatorial cooling with a maximum in the EEP reaching −5°C, and the thermocline deepens more than 20 m in the western equatorial Pacific. The enhanced equatorial cooling at the LGM is opposite to the enhanced equatorial warming under a global warming case [*Liu et al.*, 2005], likely suggesting a similar causal mechanism through the GHG forcing. The maximum equatorial cooling of −5°C is larger than the mean value in previous simulations [*Otto-Bliesner et al.*, 2009; *Brady et al.*, 2013], and a recent compilation

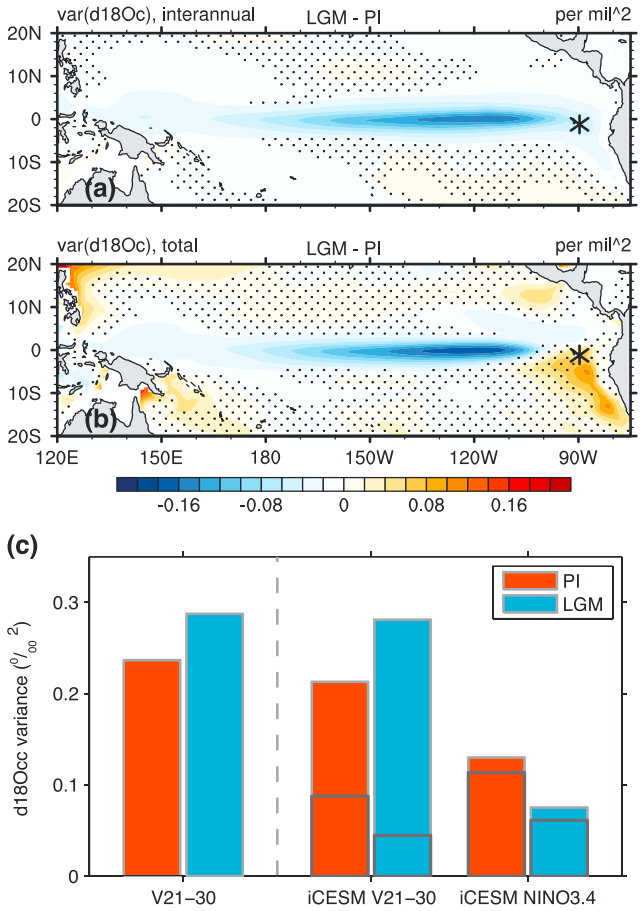

Figure 2. (a) Changes in variance of $\delta^{18}O_c$ at interannual time scale calculated from model results (LGM minus preindustrial, units: ‰^{2}). Differences insignificant at the 95% confidence level are dotted. (b) Same as in Figure 2a but for the total variance. (c) Total variance for preindustrial (red) and the LGM (blue) at Core V21–30 from reconstruction (first two bars), in the model (two bars in the middle), and modeled values averaged in the Niño3.4 region (last two bars). Variance at interannual time scale (after removing the annual cycle) is also shown as black boxes. Asterisks in Figures 2a and 2b denote the location of core site V21–30.

of proxy data [*Waelbroeck et al.*, 2009], as well as a model-data synthesis [*Annan and Hargreaves*, 2013]. This cooling is, however, within the uncertainty range of the data [*Waelbroeck et al.*, 2009; *Annan and Hargreaves*, 2013] (Figure S1 and Text S2 in the supporting information). We note that the La Niña-like cooling pattern with an increased zonal temperature gradient is also within the uncertainties of the currently available reconstructions [*Waelbroeck et al.*, 2009; *Annan and Hargreaves*, 2013]. Moreover, a clear reverse relationship between the annual cycle and ENSO variability in the EEP is not found in the present study (Figure S2 and Text S3).

4. Comparison With the IFA Records

Next, we move onto directly comparing model results against reconstructions of the LGM ENSO in the EEP, namely, the foraminiferal $\delta^{18}O$ records at the Cores V21–30 (1°13′S, 89°41′W) [*Koutavas and Joanides*, 2012], CD38-17P (1°36′S, 90°25′W) [*Sadekov et al.*, 2013], and MD02–2529 (8°12′N, 84°07′W) [*Leduc et al.*, 2009]. Those $\delta^{18}O$ records employ a method called the individual foraminifera analysis (IFA), which involves measuring the $\delta^{18}O$ of individual foraminifera shells ($\delta^{18}O_c$). For example, about 50–80 of surface-dwelling *Globigerinoides ruber* or subsurface-dwelling *Neogloboquadrina dutertrei* shells are picked for the late Holocene and the LGM from narrow intervals of ocean sediments with time windows dependent on the sedimentation rate at the site (typically ~100 years). If a reduced sample variance of $\delta^{18}O_c$ of the LGM shells is observed comparing to the available core-top one, then it is concluded that ENSO is reduced and vice versa. The surface core V21–30 and subsurface core CD38-17P exhibit increased total variance of $\delta^{18}O_c$ and have been interpreted as strengthened ENSO variability [*Koutavas and Joanides*, 2012; *Sadekov et al.*, 2013]. On the other hand, the subsurface core MD02–2529 shows decreased total variance and weakened ENSO [*Leduc et al.*, 2009]. However, there could be considerable uncertainty associated with these $\delta^{18}O$-IFA records, including the difference between the total and interannual variances [*Thirumalai et al.*, 2013], vertical migration of the foraminifera [*Sautter and Thunell*, 1991; *Field*, 2004], variations in the isotope composition of seawater ($\delta^{18}O_w$) [*Russon et al.*, 2013], the intershell variability, and changes in seasonality of sedimentation rate [*Hemleben et al.*, 2012]. Fortunately, with an isotope-enabled Earth system model, we can directly compare model results with these reconstructions and, therefore, assess some of the uncertainties associated with the IFA approach.

Changes of the interannual and total variance (including interannual and annual variances) of $\delta^{18}O_c$ at the ocean surface between the LGM and preindustrial simulations, and the comparison with the surface

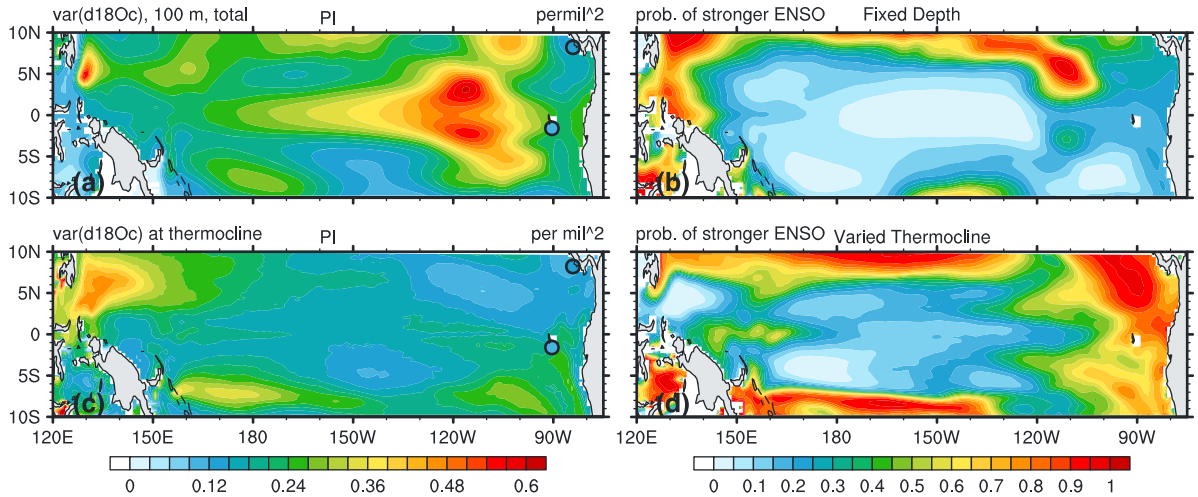

Figure 3. (a) Total variance of $\delta^{18}O_c$ at 100 m depth in preindustrial simulation (units: ‰^{2}). (b) Same as in Figure 3a but for the total variance at temporally varying thermocline. (c) Probability of getting a stronger LGM ENSO calculated from a Monte Carlo method assuming foraminifera live at a fixed depth (100 m). (d) Same as in Figure 3c but assuming that foraminifera migrate vertically with the upwelling/downwelling ocean environment. The circles in Figures 3a and 3c denote the location of core sites MD02–2529 and CD38-17P, respectively.

reconstruction at the Core V21–30, are shown in Figure 2. Our isotope-enabled simulations demonstrate that changes of variance associated with ENSO variability can be significantly different from the total variance when the seasonal cycle is included, especially in the EEP where they can be of the opposite sign (Figures 2a and 2b). The model can reproduce the increased total variance at the Core V21–30 remarkably well (Figure 2c): a 33% increase of total variance (from 0.21 to 0.28‰^{2}) in the model versus a 22% increase (from 0.23 to 0.28‰^{2}) in the reconstructions [*Koutavas and Joanides*, 2012]. Despite the original interpretation of an increased ENSO variability at the LGM, the calculation of interannual variability (by removing the annual cycle) in the model suggests otherwise. After removing the annual cycle, the model shows a dramatic decrease of interannual variance by 56%, suggesting that the increased total variance is produced by an enhanced annual cycle instead of a stronger ENSO variability. The enhanced annual cycle could be caused by the large LGM ice sheets [*Lu et al.*, 2016]. This opposite sign of changes in the total and interannual variances does exist not only at the Core V21–30 but also in broader regions in the south- and north-eastern equatorial Pacific (Figures 2a and 2b), as well as the subsurface EEP (Figures S3 and S4 and Text S4). Therefore, our results compare well with the surface IFA record at the Core V21–30 and demonstrate that changes in total variance do not always reflect changes of the ENSO variability in the EEP for both surface and subsurface records, which is consistent with speculations in previous studies [*Thirumalai et al.*, 2013; *Ford et al.*, 2015].

Given the tendency of subsurface foraminifera (e.g., *N. dutertrei*) to migrate up and down with temporally varying thermocline at seasonal and longer time scales [*Sautter and Thunell*, 1991; *Field*, 2004], we first compare the variance of $\delta^{18}O_c$ documented at a fixed depth (a Eulerian view; Figure 3a) with that recorded along a temporally varying thermocline (a Lagrangian view; Figure 3c). We find that the two variances are fundamentally different. At a fixed depth, the variabilities associated with the ENSO and annual cycle are well captured, while at the temporally varying thermocline, these variabilities are filtered out, as temperature and $\delta^{18}O_c$ changes are closely tied with deepening and shoaling of the thermocline. Consequently, the subsurface foraminifera could only record a background variability, if they migrate perfectly with the vertical variation of the thermocline. In reality, the signal recorded is likely a mixture of these two views, capturing part of the ENSO and annual cycle and part of the background variability. Here we argue that a detailed model-data comparison is not useful (Figures S4 and S5, Table S2, and Text S5) unless we have a better understanding about the regional/local hydrological characteristics at coring sites which ultimately shape the vertical distribution of planktonic foraminifera. Because of its representativeness of thermocline along the equatorial Pacific, 100 m is chosen here to calculate the variance at fixed depth. Major results here do not depend on the depth chosen (Figure S5).

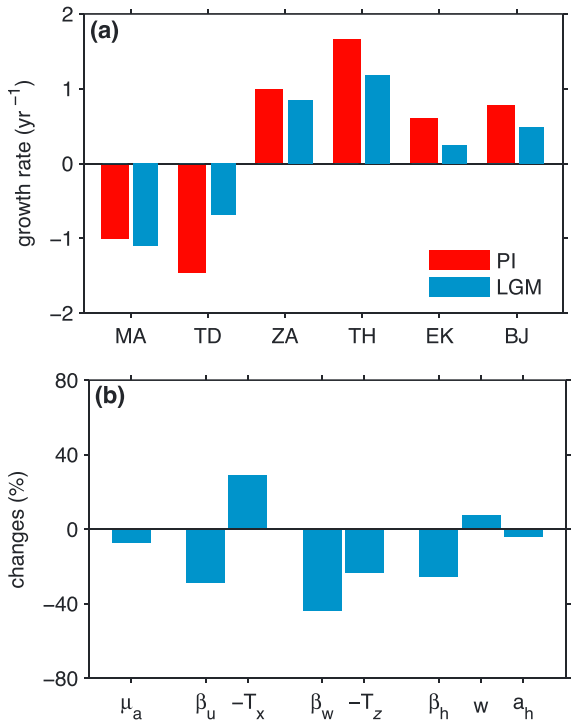

Figure 4. (a) BJ index for preindustrial and LGM simulations. MA, TD, ZA, TH, and EK denote the mean advection, thermal damping, zonal advection, thermocline, and Ekman pumping feedback, respectively. (b) Changes in percentage of different regression coefficients and mean temperature gradients.

Nevertheless, the uncertainty associated with the IFA records using the thermocline-dwelling species, considering the spread of their habitat depth [*Hemleben et al.*, 2012] and the possible migration with varying ocean environments [*Sautter and Thunell*, 1991; *Field*, 2004], can still be assessed in the model by applying a Monte Carlo approach. We assume the habitat depth of *N. dutertrei* has a spread of 20 m around a fixed depth or a temporally varying thermocline [*Sautter and Thunell*, 1991; *Field*, 2004; *Hemleben et al.*, 2012]. We then randomly draw 60 samples of $\delta^{18}O_c$ with replacement from this habitat zone from 100 year model data of the preindustrial and LGM simulations, respectively. The procedure is repeated 10,000 times and then statistics of sample variance are compared. Although the truth in the model is a weaker ENSO strength at the LGM, there is still a substantial chance that the IFA "reconstructions" using model data could result in an enhanced glacial ENSO (a false signal) for both the Eulerian and Lagrangian views (Figures 3b and 3d). Results reveal that, even if all the subsurface foraminifera strictly live at a fixed depth (e.g., 100 m; see also calculations for 50 m in Figure S5), there is still considerable probability (>10%) that the IFA records in the EEP incorrectly show a stronger ENSO at the LGM. The probability of a false signal increases substantially if the subsurface foraminifera migrate with the shoaling and deepening of thermocline. Overall, the large probability of the IFA yielding a false result could be caused by a limited sample size, the increased subsurface annual cycle, a large range of the habitat depth, and the tendency to migrate with the temporally varying thermocline depth.

5. Mechanisms in the Model and Implications for Global Warming

To understand the mechanisms for the weakened ENSO at the LGM in the model, the Bjerknes (BJ) stability index [*Jin et al.*, 2006] is calculated for the EEP. The BJ index captures the growth rate of ENSO variability and quantifies the contribution of coupled atmosphere-ocean feedback, including the positive feedback of the zonal advection, thermocline, and Ekman pumping, as well as the negative feedback of the mean advection and thermal damping [*Jin et al.*, 2006; *Z. Liu et al.*, 2014]. Figure 4a shows that, consistent with the weakened ENSO at the LGM, the total BJ index is also much smaller (by 38%). A further decomposition attributes this reduction in BJ index mostly to the decreased positive feedback, namely, the Ekman pumping, thermocline, and zonal advection feedback. The weakened Ekman pumping feedback is caused by both the reduced mean thermal stratification ($-T_z$ in Figure 4b) and the decreased sensitivity of anomalous upwelling to anomalous surface wind stress (β_w). The reduced sensitivity of the thermocline depth (β_h) (and in turn, the entrainment of subsurface warm anomalies to the surface) to anomalous wind stress is the primary cause for the decreased thermocline feedback. Although there is a stronger zonal temperature gradient (the La Niña-like cooling in Figure 1d), which favors a stronger zonal advection feedback at the LGM, its effect is outweighed by the decreased sensitivity of anomalous zonal current to the surface wind stress (β_u). The generally reduced sensitivity of the ocean dynamic response to surface wind anomalies could be a result of the deepened thermocline in a colder climate, e.g., the increased thermodynamic and dynamic inertia.

Additional sensitivity experiments suggest that the decreased BJ index and the weakened ENSO strength at the LGM is primarily caused by the lowered concentrations of GHGs, and secondly by the presence of large extensive glacial ice sheets (Figures S6 and S7 and Text S6). In a further sensitivity experiment of doubling the atmospheric CO_2, both the BJ index and ENSO strength increase significantly (Figure S6e). These results suggest a positive relationship between the ENSO strength and GHG concentrations, and a stronger ENSO under global warming.

6. Conclusions and Discussion

In summary, our modeling results using the isotope-enabled CESM suggest that the ENSO strength at the LGM is about 30% weaker than that of the preindustrial, primarily attributable to the weakened ocean-atmosphere coupled feedback in a colder climate with a deeper thermocline. The increased total variance of surface oxygen isotopes at the LGM in one IFA record (the Core V21–30) in the EEP can be reproduced remarkably well in the model, but model results suggest that it is caused by the increased annual cycle rather than the enhanced ENSO variability as previously interpreted [*Koutavas and Joanides*, 2012]. These findings imply that the total variance of the δ^{18}O-IFA records in the EEP (both surface and subsurface) may not be used as a qualitative proxy to represent the ENSO variability. With the water-isotope capability, the model further suggests that the subsurface IFA records could be substantially uncertain because of the large range of the habitat depth of thermocline-dwelling species and the tendency to migrate with the temporally varying thermocline depth.

Interestingly, our modeling results agree well with recent Mg/Ca-based IFA-temperature records [*Ford et al*., 2015]. Their reconstructions exhibit reduced ENSO variability at the LGM associated with a deeper equatorial thermocline. Their analysis on the data from site V21–30 suggests that the increased variability reflects enhanced seasonality during the LGM. They also point out that *N. dutertrei* might have occupied a shallower portion of the thermocline at the LGM. The general similar conclusions from a totally different perspective show further consistency with our model results.

The model biases in simulating the background climate and the interannual variability in iCESM could influence findings in this study. However, it is not clear how these biases could impact the ENSO response to external forcing [*Collins et al*., 2010; *Capotondi et al*., 2015], as ENSO variability is controlled by a delicate balance of amplifying and damping feedback. A previous version of CESM with a higher-resolution (~1°) atmospheric component and improved ENSO simulation also reported weakened ENSO variability at the LGM [*Brady et al*., 2013]. Furthermore, processed-based metric analyses suggest that CESM can simulate the relative contributions of coupled ocean-atmosphere feedback reasonably well [*Bellenger et al*., 2014; *Kim et al*., 2014], which are key for simulating a correct response to external forcing [*IPCC et al*., 2013]. Both findings are consistent with what we show here.

So far, the ENSO strength at the LGM is still open to debate in reconstructions, with several paleoclimate records suggesting weakened [*Tudhope*, 2001; *Leduc et al*., 2009; *Wolff et al*., 2011; *Ford et al*., 2015] while two showing enhanced ENSO variability [*Koutavas and Joanides*, 2012; *Sadekov et al*., 2013]. Of the two IFA records signaling enhanced ENSO, our isotope-enabled simulations suggest that one could merely reflect changes in the annual cycle instead of ENSO variability [*Koutavas and Joanides*, 2012] and the other is subject to substantial complications from the habitat depth of the thermocline-dwelling foraminifera [*Sadekov et al*., 2013]. As a result, the reconstructions overall may show a weaker ENSO at the LGM, agreeing qualitatively with our iCESM simulation as well as the multimodel median of the recent generation of climate models [*IPCC et al*., 2013]. Therefore, by directly comparing the isotope-enabled model results against reconstructions for the first time and combining evidence from both ends, we conclude that the ENSO strength at the LGM is most likely weaker than that at the preindustrial. This may suggest that the ENSO strength under global warming could be stronger, opposite to the weaker ENSO under the glacial global cooling. More studies with different isotope-enabled climate models and new paleorecords are urgently needed in order to further constrain the current uncertainties.

Acknowledgments
This work is supported by NSF, DOE. We thank David Bailey, Erik Kluzek, and Mariana Vertenstein for the help on developing and testing the iCESM. We would like to acknowledge high-performance computing support from Yellowstone (ark:/85065/d7wd3xhc) provided by NCAR's Computational and Information Systems Laboratory, sponsored by the National Science Foundation. The iCESM model codes are available through the National Center for Atmospheric Research software development repository. Data for simulations in this paper can be requested by sending e-mail to J.Z. (jzhu47@wisc.edu).

References

Annan, J. D., and J. C. Hargreaves (2013), A new global reconstruction of temperature changes at the Last Glacial Maximum, *Clim. Past*, *9*(1), 367–376, doi:10.5194/cp-9-367-2013.

Bellenger, H., E. Guilyardi, J. Leloup, M. Lengaigne, and J. Vialard (2014), ENSO representation in climate models: From CMIP3 to CMIP5, *Clim. Dyn.*, *42*(7), 1999–2018, doi:10.1007/s00382-013-1783-z.

Bemis, B. E., H. J. Spero, J. Bijma, and D. W. Lea (1998), Reevaluation of the oxygen isotopic composition of planktonic foraminifera: Experimental results and revised paleotemperature equations, *Paleoceanography*, *13*(2), 150–160, doi:10.1029/98PA00070.

Brady, E. C., B. L. Otto-bliesner, J. E. Kay, and N. Rosenbloom (2013), Sensitivity to glacial forcing in the CCSM4, *J. Clim.*, *26*(6), 1901–1925, doi:10.1175/JCLI-D-11-00416.1.

Capotondi, A., Y.-G. Ham, A. T. Wittenberg, and J.-S. Kug (2015), Climate model biases and El Niño Southern Oscillation (ENSO) simulation, *US CLIVAR Var.*, *13*(1), 21–25.

Carre, M., J. P. Sachs, S. Purca, A. J. Schauer, P. Braconnot, R. A. Falcon, M. Julien, and D. Lavallee (2014), Holocene history of ENSO variance and asymmetry in the eastern tropical Pacific, *Science*, *345*(6200), 1045–1048, doi:10.1126/science.1252220.

Clark, P. U., A. S. Dyke, J. D. Shakun, A. E. Carlson, J. Clark, B. Wohlfarth, J. X. Mitrovica, S. W. Hostetler, and A. M. McCabe (2009), The Last Glacial Maximum, *Science*, *325*(5941), 710 LP-714.

Clement, A. C., R. Seager, and M. A. Cane (1999), Orbital controls on the El Niño/Southern Oscillation and the tropical climate, *Paleoceanography*, *14*(4), 441, doi:10.1029/1999PA900013.

Cobb, K. M., C. D. Charles, H. Cheng, and R. L. Edwards (2003), El Niño/Southern Oscillation and tropical Pacific climate during the last millennium, *Nature*, *424*(6946), 271–276, doi:10.1038/nature01779.

Cobb, K. M., N. Westphal, H. R. Sayani, J. T. Watson, E. Di Lorenzo, H. Cheng, R. L. Edwards, and C. D. Charles (2013), Highly variable El Niño-Southern Oscillation throughout the Holocene, *Science*, *339*(6115), 67–70, doi:10.1126/science.1228246.

Collins, M. et al. (2010), The impact of global warming on the tropical Pacific Ocean and El Niño, *Nat. Geosci.*, *3*(6), 391–397, doi:10.1038/NGEO868.

Deser, C., A. S. Phillips, R. A. Tomas, Y. M. Okumura, M. A. Alexander, A. Capotondi, J. D. Scott, Y. O. Kwon, and M. Ohba (2012), ENSO and pacific decadal variability in the Community Climate System Model version 4, *J. Clim.*, *25*(8), 2622–2651, doi:10.1175/JCLI-D-11-00301.1.

DiNezio, P. N., A. Timmermann, J. E. Tierney, F. F. Jin, B. Otto-Bliesner, N. Rosenbloom, B. Mapes, R. Neale, R. F. Ivanovic, and A. Montenegro (2016), The climate response of the Indo-Pacific warm pool to glacial sea level, *Paleoceanography*, *31*, 866–894, doi:10.1002/2015PA002890.

Duplessy, J. C., L. Labeyrie, and C. Waelbroeck (2002), Constraints on the ocean oxygen isotopic enrichment between the Last Glacial Maximum and the Holocene: Paleoceanographic implications, *Quat. Sci. Rev.*, *21*(1–3), 315–330, doi:10.1016/S0277-3791(01)00107-X.

Fedorov, A. V., and S. G. Philander (2001), A stability analysis of tropical ocean-atmosphere interactions: Bridging measurements and theory for El Niño, *J. Clim.*, *14*(14), 3086–3101, doi:10.1175/1520-0442(2001)014<3086:ASAOTO>2.0.CO;2.

Field, D. B. (2004), Variability in vertical distributions of planktonic foraminifera in the California current: Relationships to vertical ocean structure, *Paleoceanography*, *19*, PA2014, doi:10.1029/2003PA000970.

Ford, H. L., A. C. Ravelo, and P. J. Polissar (2015), Reduced El Niño–Southern Oscillation during the Last Glacial Maximum, *Science*, *347*(6219), 255–258, doi:10.1126/science.1258437.

Freeman, E., et al. (2017), ICOADS release 3.0: A major update to the historical marine climate record, *Int. J. Climatol.*, *37*(5), 2211–2232, doi:10.1002/joc.4775.

Hemleben, C., M. Spindler, and O. R. Anderson (2012), *Modern Planktonic Foraminifera*, pp. 220–257, Springer, New York.

Huang, B., V. F. Banzon, E. Freeman, J. Lawrimore, W. Liu, T. C. Peterson, T. M. Smith, P. W. Thorne, S. D. Woodruff, and H.-M. Zhang (2014), Extended Reconstructed Sea Surface Temperature version 4 (ERSST.v4). Part I: Upgrades and Intercomparisons, *J. Clim.*, *28*(3), 911–930, doi:10.1175/JCLI-D-14-00006.1.

Hurrell, J. W., et al. (2013), The Community Earth System Model: A framework for collaborative research, *Bull. Am. Meteorol. Soc.*, *94*(9), 1339–1360, doi:10.1175/BAMS-D-12-00121.1.

IPCC, et al. (2013), *Climate Change 2013: The Physical Science Basis*, edited by T. F. Stocker et al., pp. 741–866, Cambridge Univ. Press, Cambridge, U. K., and New York.

Jin, F.-F., S. T. Kim, and L. Bejarano (2006), A coupled-stability index for ENSO, *Geophys. Res. Lett.*, *33*, L23708, doi:10.1029/2006GL027221.

Kageyama, M., et al. (2016), PMIP4-CMIP6: The contribution of the Paleoclimate Modelling Intercomparison Project to CMIP6, *Geosci. Model Dev. Discuss.*, 1–46, doi:10.5194/gmd-2016-106, in press.

Karnauskas, K. B., J. E. Smerdon, R. Seager, and J. F. González-Rouco (2012), A Pacific Centennial Oscillation predicted by coupled GCMs, *J. Clim.*, *25*(17), 5943–5961, doi:10.1175/JCLI-D-11-00421.1.

Kim, S. T., W. Cai, F.-F. Jin, A. Santoso, L. Wu, E. Guilyardi, and S.-I. An (2014), Response of El Niño sea surface temperature variability to greenhouse warming, *Nat. Clim. Change*, *4*(September), 1–5, doi:10.1038/nclimate2326.

Koutavas, A., and S. Joanides (2012), El Niño-Southern Oscillation extrema in the Holocene and Last Glacial Maximum, *Paleoceanography*, *27*, PA4208, doi:10.1029/2012PA002378.

Leduc, G., L. Vidal, O. Cartapanis, and E. Bard (2009), Modes of eastern equatorial Pacific thermocline variability: Implications for ENSO dynamics over the last glacial period, *Paleoceanography*, *24*, PA3202, doi:10.1029/2008PA001701.

LeGrande, A. N., and G. A. Schmidt (2006), Global gridded data set of the oxygen isotopic composition in seawater, *Geophys. Res. Lett.*, *33*, L12604, doi:10.1029/2006GL026011.

Liu, W., B. Huang, P. W. Thorne, V. F. Banzon, H.-M. Zhang, E. Freeman, J. Lawrimore, T. C. Peterson, T. M. Smith, and S. D. Woodruff (2014), Extended Reconstructed Sea Surface Temperature version 4 (ERSST.v4): Part II. Parametric and structural uncertainty estimations, *J. Clim.*, *28*(3), 931–951, doi:10.1175/JCLI-D-14-00007.1.

Liu, Z., and M. Alexander (2007), Atmospheric bridge, oceanic tunnel, and global climatic teleconnections, *Rev. Geophys.*, *45*, RG2005, doi:10.1029/2005RG000172.

Liu, Z., S. Vavrus, F. He, N. Wen, and Y. Zhong (2005), Rethinking tropical ocean response to global warming: The enhanced equatorial warming, *J. Clim.*, *18*(22), 4684–4700, doi:10.1175/JCLI3579.1.

Liu, Z., Z. Lu, X. Wen, B. L. Otto-Bliesner, A Timmermann, and K. M. Cobb (2014), Evolution and forcing mechanisms of El Niño over the past 21,000 years, *Nature*, *515*(7528), 550–553, doi:10.1038/nature13963.

Lu, Z., Z. Liu, and J. Zhu (2016), Abrupt intensification of ENSO forced by deglacial ice-sheet retreat in CCSM3, *Clim. Dyn.*, *46*(5–6), 1877–1891, doi:10.1007/s00382-015-2681-3.

Nusbaumer, J., T. Wong, C. Bardeen, and D. Noone (2017), Evaluating hydrological processes in the Community Atmosphere Model version 5 (CAM5) using stable isotope ratios of water, *J. Adv. Model. Earth Syst.*, doi: 10.1002/2016MS000839, in press.

Otto-Bliesner, B. L. (2003), Modeling El Niño and its tropical teleconnections during the last glacial-interglacial cycle, *Geophys. Res. Lett.*, *30*(23), 2198, doi:10.1029/2003GL018553.

Otto-Bliesner, B. L., E. C. Brady, G. Clauzet, R. Tomas, S. Levis, and Z. Kothavala (2006), Last Glacial Maximum and Holocene climate in CCSM3, *J. Clim.*, *19*(11), 2526–2544, doi:10.1175/JCLI3748.1.

Otto-Bliesner, B. L., et al. (2009), A comparison of PMIP2 model simulations and the MARGO proxy reconstruction for tropical sea surface temperatures at Last Glacial Maximum, *Clim. Dyn.*, *32*(6), 799–815, doi:10.1007/s00382-008-0509-0.

Peltier, W. R., D. F. Argus, and R. Drummond (2015), Space geodesy constrains ice age terminal deglaciation: The global ICE-6G_C (VM5a) model, *J. Geophys. Res. Solid Earth*, *120*, 450–487, doi:10.1002/2014JB011176.

Philander, S. G. (1990), *El Niño, La Niña, and the Southern Oscillation*, vol. 9, 293 pp., Academic Press, San Diego, Calif.

Ravelo, A. C., and C. Hillaire-Marcel (2007), The use of oxygen and carbon isotopes of foraminifera in paleoceanography, in *Developments in Marine Geology*, vol. 1, edited by H. Claude and V. Anne De, pp. 735–763, Elsevier, Amsterdam, Netherlands.

Risien, C. M., and D. B. Chelton (2008), A global climatology of surface wind and wind stress fields from eight years of QuikSCAT Scatterometer data, *J. Phys. Oceanogr.*, *38*(11), 2379–2413, doi:10.1175/2008JPO3881.1.

Russon, T., A. W. Tudhope, G. C. Hegerl, M. Collins, and J. Tindall (2013), Inter-annual tropical Pacific climate variability in an isotope-enabled CGCM: Implications for interpreting coral stable oxygen isotope records of ENSO, *Clim. Past*, *9*(4), 1543–1557, doi:10.5194/cp-9-1543-2013.

Sadekov, A. Y., R. Ganeshram, L. Pichevin, R. Berdin, E. McClymont, H. Elderfield, and A. W. Tudhope (2013), Palaeoclimate reconstructions reveal a strong link between El Niño–Southern Oscillation and tropical Pacific mean state, *Nat. Commun.*, *4*, 2692, doi:10.1038/ncomms3692.

Sautter, L. R., and R. C. Thunell (1991), Seasonal variability in the $\delta^{18}O$ and $\delta^{13}C$ of planktonic foraminifera from an upwelling environment: Sediment trap results from the San Pedro Basin, Southern California Bight, *Paleoceanography*, *6*(3), 307–334, doi:10.1029/91PA00385.

Shackleton, N. J. (1974), Attainment of isotopic equilibrium between ocean water and the benthonic foraminifera genus *Uvigerina*: Isotopic changes in the ocean during the last glacial, *Colloq. Int. du C.N.R.S.*, *219*, 203–210.

Small, R. J., et al. (2014), A new synoptic scale resolving global climate simulation using the Community Earth System Model, *J. Adv. Model. Earth Syst.*, *6*(4), 1065–1094, doi:10.1002/2014MS000363.

Thirumalai, K., J. W. Partin, C. S. Jackson, and T. M. Quinn (2013), Statistical constraints on El Niño Southern Oscillation reconstructions using individual foraminifera: A sensitivity analysis, *Paleoceanography*, *28*, 401–412, doi:10.1002/palo.20037.

Tudhope, A. (2001), Variability in the El Niño Southern Oscillation through the glacial-interglacial cycle, *Science*, *291*(2001), 1511–1517, doi:10.1126/science.1057969.

Waelbroeck, C., et al. (2009), Constraints on the magnitude and patterns of ocean cooling at the Last Glacial Maximum, *Nat. Geosci.*, *2*(2), 127–132, doi:10.1038/ngeo411.

Wang, B., and S. I. An (2002), A mechanism for decadal changes of ENSO behavior: Roles of background wind changes, *Clim. Dyn.*, *18*(6), 475–486, doi:10.1007/s00382-001-0189-5.

Wolff, C., G. H. Haug, A. Timmermann, J. S. Sinninghe Damsté, A. Brauer, D. M. Sigman, M. A. Cane, and D. Verschuren (2011), Reduced interannual rainfall variability in East Africa during the last ice age, *Science*, *333*(6043), 743–747, doi:10.1126/science.1203724.

Wong, T., J. Nusbaumer, and D. Noone (2017), Evaluation of modeled land-atmosphere exchanges with a comprehensive water isotope fractionation scheme in version 4 of the Community Land Model, *J. Adv. Model. Earth Syst.*, doi:10.1002/2016MS000842, in press.

Yang, H., and F. Wang (2009), Revisiting the thermocline depth in the equatorial Pacific, *J. Clim.*, *22*(13), 3856–3863, doi:10.1175/2009JCLI2836.1.

Zhang, J. (2016), Understanding the deglacial evolution of deep Atlantic water masses in an isotope-enabled ocean model, PhD thesis, Univ. of Wisconsin-Madison.

Zheng, W., P. Braconnot, E. Guilyardi, U. Merkel, and Y. Yu (2008), ENSO at 6 ka and 21 ka from ocean-atmosphere coupled model simulations, *Clim. Dyn.*, *30*(7–8), 745–762, doi:10.1007/s00382-007-0320-3.